

## 2D properties of core turbulence on DIII-D and comparison to gyrokinetic simulations

Cite as: Phys. Plasmas **19**, 032504 (2012); <https://doi.org/10.1063/1.3691965>

Submitted: 17 November 2011 • Accepted: 13 February 2012 • Published Online: 15 March 2012

M. W. Shafer, R. J. Fonck, G. R. McKee, et al.



View Online



Export Citation

### ARTICLES YOU MAY BE INTERESTED IN

[Effects of E×B velocity shear and magnetic shear on turbulence and transport in magnetic confinement devices](#)

[Physics of Plasmas \*\*4\*\*, 1499 \(1997\); https://doi.org/10.1063/1.872367](#)

[Spatial transfer function for the beam emission spectroscopy diagnostic on DIII-D](#)

[Review of Scientific Instruments \*\*77\*\*, 10F110 \(2006\); https://doi.org/10.1063/1.2221908](#)

[Electron temperature gradient driven turbulence](#)

[Physics of Plasmas \*\*7\*\*, 1904 \(2000\); https://doi.org/10.1063/1.874014](#)



**Physics of Plasmas   Physics of Fluids**  
Special Topic: Turbulence in Plasmas and Fluids  
[Submit Today!](#)

## 2D properties of core turbulence on DIII-D and comparison to gyrokinetic simulations

M. W. Shafer,<sup>1</sup> R. J. Fonck,<sup>2</sup> G. R. McKee,<sup>2</sup> C. Holland,<sup>3</sup> A. E. White,<sup>4</sup> and D. J. Schlossberg<sup>2</sup>

<sup>1</sup>Oak Ridge National Laboratory, Oak Ridge, Tennessee 37831-6372, USA

<sup>2</sup>University of Wisconsin-Madison, Madison, Wisconsin 53706, USA

<sup>3</sup>University of California-San Diego, San Diego, California 92093, USA

<sup>4</sup>Massachusetts Institute of Technology, Cambridge, Massachusetts 02139, USA

(Received 17 November 2011; accepted 13 February 2012; published online 15 March 2012)

Quantitative 2D characteristics of localized density fluctuations are presented over the range of  $0.3 < r/a < 0.9$  in L-mode plasmas on DIII-D [J. L. Luxon, Nucl. Fusion **42**, 614 (2002)]. Broadband density fluctuations increase in amplitude from  $\tilde{n}/n < 0.5\%$  in the deep core to  $\tilde{n}/n \sim 2.5\%$  near the outer region. The observed Doppler-shift due to the  $\mathbf{E} \times \mathbf{B}$  velocity matches well with the measured turbulence group and phase velocities (in toroidally rotating neutral beam heated plasmas). Turbulence decorrelation rates are found to be  $\sim 200$  kHz at the edge and to decrease toward the core ( $0.45 < r/a < 0.9$ ) where they approach the  $\mathbf{E} \times \mathbf{B}$  shearing rate ( $\sim 50$  kHz). Radial and poloidal correlation lengths are found to scale with the ion gyroradius and exhibit an asymmetric poloidally elongated eddy structure. The ensemble-averaged turbulent eddy structure changes its tilt with respect to the radial-poloidal coordinates in the core, consistent with an  $\mathbf{E} \times \mathbf{B}$  shear mechanism. The 2D spatial correlation and wavenumber spectra [ $S(k_r, k_\theta)$ ] are presented and compared to nonlinear flux-tube GYRO simulations at two radii,  $r/a = 0.5$  and  $r/a = 0.75$ , showing reasonable overall agreement, but the GYRO spectrum exhibits a peak at finite  $k_r$  for  $r/a = 0.75$  that is not observed experimentally;  $\mathbf{E} \times \mathbf{B}$  shear may cause this discrepancy. © 2012 American Institute of Physics. [<http://dx.doi.org/10.1063/1.3691965>]

### I. INTRODUCTION

Confinement of high-pressure tokamak plasmas, suitable for fusion energy, are limited by anomalously high energy and particle transport, which is attributed to small-scale turbulent instabilities.<sup>1</sup> Pressure-gradient driven drift-wave turbulence modes have been theorized to cause such transport in the core of a magnetically confined over a wide range of spatial scales, which include ion temperature gradient (ITG),  $k_\perp \rho_i \leq 1$ , trapped electron mode (TEM),  $k_\perp \rho_i \sim 1$ , and electron temperature gradient (ETG),  $k_\perp \rho_i \gg 1$ , where  $k_\perp$  is the perpendicular wavenumber and  $\rho_i$  is the ion gyro radius ( $\rho_i \equiv \sqrt{m_i T_i / eB}$ ).<sup>2</sup> These instabilities are inherently three-dimensional. However, since  $k_{||} \rho_i \ll 1$ , the crucial dynamics governing cross-field transport occur in the 2D radial/poloidal plane. Thus, understanding the underlying turbulence instabilities in these relevant dimensions benefits from 2D measurements.

Turbulence measurements in the core of tokamak plasmas are often limited to one dimension or are line-integrated.<sup>3</sup> Some quantitative 2D turbulence measurements have been obtained in the edge, but 2D measurements in the core of a high-temperature tokamak plasmas are very limited. Gas puff imaging provides high spatial and temporal resolution 2D measurements of  $\tilde{n}/n$ , in the edge regions.<sup>4</sup> A number of low-temperature devices make use of Langmuir probe arrays for density ( $\tilde{n}/n$ ) and potential ( $\tilde{\phi}/\phi$ ) fluctuation measurements;<sup>5–7</sup> however, such measurements are usually taken under conditions similar to those in the edge or scrape-off-layer of high-temperature tokamak plasmas.

Beam emission spectroscopy (BES) on DIII-D provides simultaneous 2D measurements of long-wavelength density fluctuations ( $k_\perp \rho_i \leq 1$ ) in the poloidal and radial directions in both the core and edge of high-temperature plasmas.<sup>8</sup> A 1D BES diagnostic was used in the core of TFTR to measure the structure of long wavelength turbulence and showed near isotropic radial and poloidal correlation lengths.<sup>9,10</sup>

In this paper, we present a detailed assessment of several relevant characteristics of localized 1D and 2D measurements of long wavelength ( $k_\perp \rho_i \leq 1$ ) density fluctuations in L-mode plasmas. These measurements are obtained in the core ( $0.3 < r/a < 0.9$ ) of the DIII-D tokamak and examine the frequency spectra, turbulence group and phase velocities, poloidal and radial correlation lengths, decorrelation rates, and 2D structure in real and wavenumber space. This collection provides a comprehensive set of long wavelength core turbulence properties. The 2D structure is further compared to gyrokinetic simulations with the GYRO code.<sup>11</sup> This experimental investigation comprehensively documents the spatiotemporal characteristics of turbulence in a L-mode discharge with a goal of understanding the impact of equilibrium  $\mathbf{E} \times \mathbf{B}$  flow—comparing the 2D wavenumber spectrum with nonlinear simulation, a key element of the simulation validation process—and potentially explaining an apparent discrepancy between measurement and simulation.

This paper is organized in the following way. First, the discharge scenario and the diagnostic setup are described. Second, the 2D analysis techniques are detailed. Third, the

1D and 2D characteristics are presented. Finally, a comparison with simulations is presented.

## II. EXPERIMENTAL SETUP

The measurements presented in this paper were obtained in low density L-mode plasmas with the following parameters:  $B_T = 2\text{ T}$ ,  $I_p = 1\text{ MA}$ ,  $\beta_n = 0.5$ , and  $P_{inj} = 2.5\text{ MW}$  of neutral beam injection (NBI). These discharges were used for a previous comparison of density and electron temperature fluctuations with GYRO simulations.<sup>12,13</sup> Time traces of plasma current  $I_p$ , injected power  $P_{inj}$ , safety factor  $q$ , electron temperature  $T_e$ , ion temperature  $T_i$ , toroidal rotation velocity  $v_\phi$ , and electron density  $n_e$  are shown in Fig. 1. The region in between vertical dashed lines indicates the time window used for ensemble-averaging of the BES fluctuation measurements. This period was chosen for relatively long duration and nearly steady-state sawtooth-free L-mode conditions. The temperature, rotation and  $q$  on axis evolve gradually towards the end of this phase. Multiple repeatable discharges were performed to obtain radial scans for complete spatial documentation of fluctuation characteristics; parameters were well matched shot to shot. The  $T_e$ ,  $T_i$ ,  $n_e$ , and  $\Omega_\phi$  profiles for the discharge in Fig. 1 are shown in Fig. 2, where  $\Omega_\phi = v_\phi/R$  is the angular toroidal rotation frequency. Here, the vertical lines indicate the region over which the BES measurements were acquired ( $0.3 < r/a < 0.9$ ). Throughout this paper,  $r/a$  is actually calculated using  $\sqrt{\psi_n}$ , where  $\psi_n$  is the normalized toroidal flux (for these low-power plasmas,  $r/a \approx \sqrt{\psi_n}$ ).

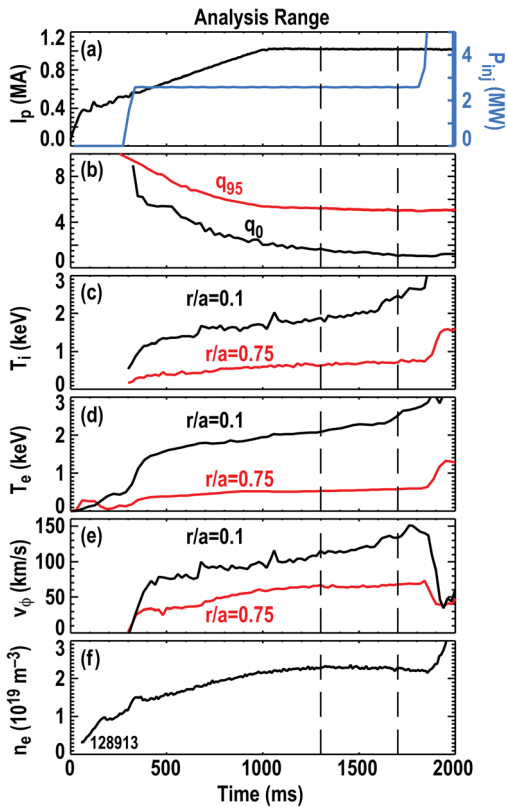


FIG. 1. (Color online) Time traces showing plasma current and neutral beam injected power (a),  $q_{95}$  and  $q_0$  (b), ion temperature (c), electron temperature (d), toroidal velocity (e), and line-averaged electron density (f). Time of interest for later analysis shown between dashed vertical lines.

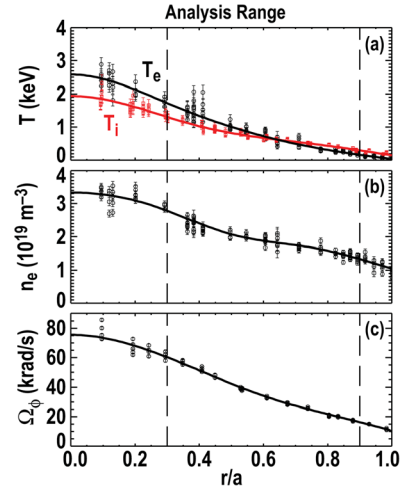


FIG. 2. (Color online) Profiles showing ion and electron temperature, red curve and black curve, respectively (a), electron density (b), and angular toroidal rotation frequency (c).

The turbulence measurements presented here were obtained with a 30-channel array of beam emission spectroscopy (BES) channels on DIII-D.<sup>8</sup> BES measures localized density fluctuations from Doppler-shifted  $D_\alpha$  ( $n = 3 \rightarrow 2$ ,  $\lambda_0 = 656.1\text{ nm}$ ) emission of collisionally excited 80 keV neutral beam atoms.<sup>14</sup> The 30 channels are arranged in a  $5 \times 6$  (radial  $\times$  poloidal) grid covering approximately  $5 \times 7\text{ cm}^2$  along the outboard midplane of the plasma. The array is translated radially on a shot-to-shot basis to acquire turbulence profiles. The array positions for the set of discharges used here are displayed with the upper single null (USN, ion  $\nabla B$  drift away from the x-point) equilibrium in Fig. 3(a). Here, the dashed contours indicate 10% increments of  $r/a$ . Figure 3(b) provides an enlarged view of the BES viewing area.

The 2D radial/poloidal sampling area is  $\sim 1\text{--}2\text{ cm}$  in each direction for a given channel and is characterized by the point spread function (PSF).<sup>15</sup> The PSF includes effects arising from the BES sightline and the neutral beam geometry, local field line pitch, and the collisionally shortened  $n = 3$  state lifetime of the excited neutral beam atom.<sup>15</sup> The  $n = 3$  lifetime is calculated via a multi-step analytic collisional-radiative model.<sup>16</sup> Accurate estimate of the PSF is needed to correct measurements for finite sample volume effects. Examples of the PSF are shown in Sec. III.

## III. ANALYSIS TECHNIQUE FOR 1D AND 2D DATA

The fluctuation measurements presented here are analyzed using standard spectral analysis techniques as well as specialized techniques specific to the nature of the fluctuation data acquired on DIII-D. Three representative power spectra at different radii are shown in Fig. 3(c), which cover the range from the deep core to the edge region. These power spectra are computed via cross-power spectral analysis via neighboring channels to remove incoherent noise. The spectra are generally very similar to auto-power spectra given the close channel spacing. The dramatic reduction in power from the edge to the core is indicative of strong edge fluctuations

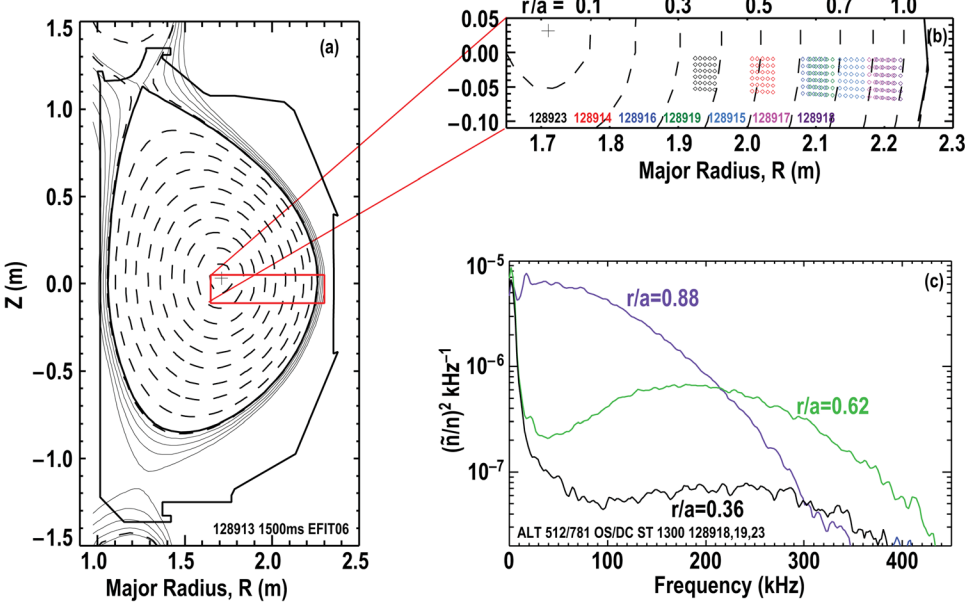


FIG. 3. (Color online) Equilibrium reconstruction (a), with enlarged view showing locations of BES channels for seven repeated discharges used in this study (b). Power spectra for three radial locations in scan (c).

and relatively weak core turbulence levels. The low-frequency peak observed most clearly in the core region is primarily a common mode artifact. The broad distribution of power over the frequency range shown is a result of Doppler shift via  $\mathbf{E} \times \mathbf{B}$  flow, which typically peaks near mid-radius.

Spatiotemporal correlation analysis is employed for both 1D and 2D data. Cross-correlations between spatially separated channels can provide estimates of eddy advection velocity, correlation lengths, and decorrelation times.<sup>17</sup> The correlation coefficient function,  $C(\Delta x, \tau)$ , is determined by

$$C(\Delta x, \tau) = \frac{\langle \tilde{I}(x, t) \tilde{I}(x + \Delta x, t + \tau) \rangle}{\sqrt{\langle \tilde{I}(x, t)^2 \rangle \langle \tilde{I}(x + \Delta x, t + \tau)^2 \rangle}},$$

where  $\tilde{I}$  is the measured fluctuating signal and  $\langle \rangle$  quantifies the ensemble average.<sup>18</sup> The envelope,  $A$ , is determined via  $A(C) = \sqrt{C^2 + H(C)^2}$ , where  $H$  is the Hilbert transform.<sup>18</sup> Figure 4 illustrates three temporally resolved correlation

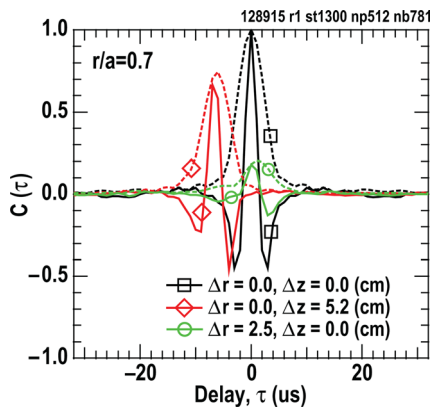


FIG. 4. (Color online) Two pair time-lag correlations. Auto-correlation (black square), cross correlation of poloidally separated channels (red diamond), cross-correlation of radially separate channels (green circle). The envelope of each is denoted by the dashed lines.

functions. In Fig. 4, an auto-correlation ( $\Delta x = 0$ ) is shown on black lines (square), a cross-correlation between vertically (radially) separated channels is shown on red lines (diamond) [green lines (circle)]. The shifted peak correlation between vertically separated channels gives an estimation of the poloidal group velocity ( $\Delta z / \tau_{\text{delay}}$ ) of the turbulence over the analysis window. For the  $5 \times 6$  BES system, a maximum of six points can be used to determine this velocity from the slope of a linear fit of delay time vs. spatial separation. Correlation lengths,  $L_c$ , are estimated as the width of a Gaussian function fitted to the envelope of the correlation function at  $\tau = 0$  vs. the distance between channels:  $A(\tau = 0) = \exp[-(x/L_c)^2]$ . The correlation time,  $\tau_c$ , is estimated as the decay constant of a fitted exponential decay to the peak correlation envelope ( $A_{\max}$ ) vs. the time of the peak correlation ( $\tau_{\text{delay}}$ ):  $A_{\max}(\tau_{\text{delay}}) = \exp(-\tau_{\text{delay}}/\tau_c)$ . The inverse of the correlation time is defined as the measured decorrelation rate,  $\tau_c^{-1}$ .

Estimation of the 2D spatial correlation function (from simultaneous radially and vertically resolved data) is constructed from multiple two-pair cross-correlations with a common reference channel across the entire array at  $\tau = 0$ . This 2D function is considered to be “raw” because it has to be corrected for the finite spatial sampling estimated by the PSF. The raw wavenumber spectrum,  $S(k_r, k_\theta)$ , is the spatial Fourier transform of the 2D correlation function. The wavenumber spectrum is corrected by deconvolution of the PSF.<sup>15</sup>

A 30-point partial image of the 2D correlation function is obtained with the current BES system. Given the typical size of the imaged turbulence, the coverage is limited to one quadrant of the full 2D correlation function. A full 2D correlation function allows a wavenumber transformation without sharp edge artifacts. An example of a 2D correlation function is illustrated in Fig. 5(a). The white crosses indicate the center of each PSF. The spacing forms a near regular grid. The color legend indicates the correlation function. The color image in Fig. 5(b) illustrates a minimum curvature spline fit to the discrete data in Fig. 5(a).

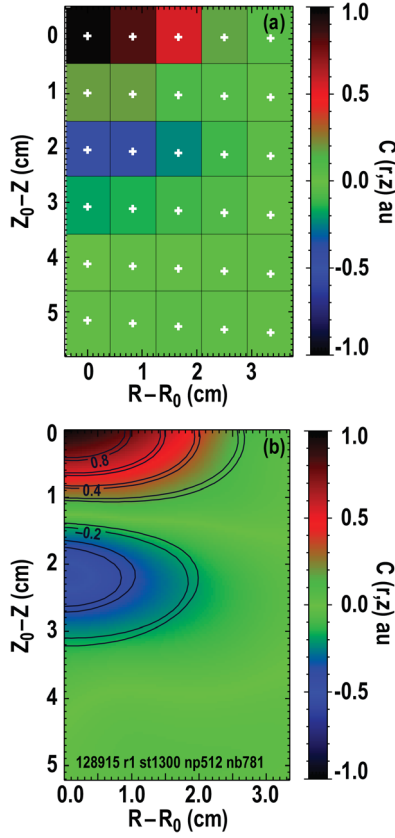


FIG. 5. (Color online) (a) 2D correlation function constructed from multiple two-pair correlations at  $\tau = 0$  with a common reference channel at  $Z = R = 0$ . Gray crosses indicate center of measurement (a). (b) Image is minimum curvature spline from data above. Contour lines represent fitted model function. Closely separated lines indicate the uncertainty.

The full 2D correlation function can be approximated with a model function. The following function is fit to the data:

$$C_{model}(r, z) = \cos(k_z|z'|^p) \exp\left[-\left(\frac{|z'|}{L_{cz'}}\right)^q - \left(\frac{|r'|}{L_{cr'}}\right)^u\right]. \quad (1)$$

Here,  $z'$  and  $r'$  are defined as

$$\begin{bmatrix} r' \\ z' \end{bmatrix} = \begin{bmatrix} 1 & 0 \\ -\tan\theta & 1 \end{bmatrix} \cdot \begin{bmatrix} r \\ z \end{bmatrix}.$$

This function characterizes the correlation function in terms of widths in the transformed coordinate space  $(r', z')$ .  $\theta$  is the estimated eddy tilt. The wavenumber in the predominantly vertical direction is characterized by  $k_z$ . The values of  $p, q, u$  are initialized at 1, 2, 2, respectively, but are allowed to vary by up to 30% to allow for slight distortions. If  $\theta$  is small ( $<10^\circ$ ) and  $p, q, u$  are equal to their initial values, the values of  $L_{cz'}$  and  $L_{cr'}$  represent an uncorrected correlation length. However, for larger values of  $\theta$  ( $|\theta| > 10^\circ$ ), the raw correlation lengths must be estimated by taking the e-folding width of the envelope of the 2D function.

This model function has been constructed as a best estimate of the data and provides a low-order approximation of the turbulence correlation function. It fits the data in Fig. 5 reasonably well. This fit uses a Levenberg-Marquardt algorithm for irregularly gridded 2D data.<sup>19</sup> The contour lines in Fig. 5(b) correspond to a model function fit to the data. The closely spaced lines indicate the uncertainty from the fit.

The accuracy of this function is further illustrated in Fig. 6 using 1D slices in the vertical and radial directions. Here, the radial direction corresponds to the lower axes in black. The vertical direction corresponds to the upper axes in red. A key in the lower right-hand corner of each plot is used to illustrate the position of the slices with respect to the reference channel (shown in the upper left corner).

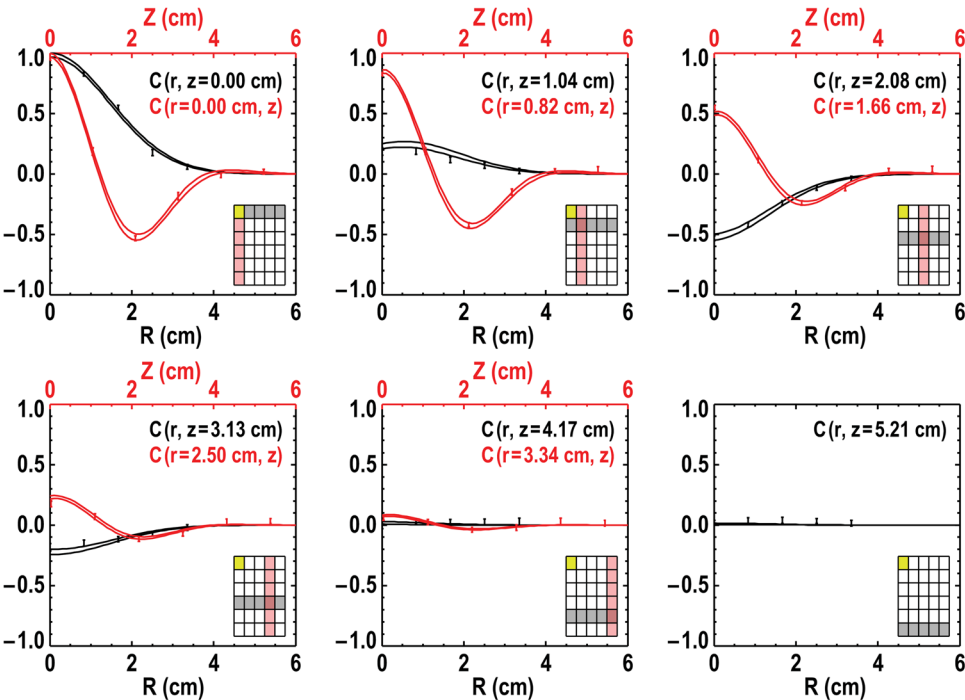


FIG. 6. (Color online) 1D slices of 2D correlation function in radial and vertical directions at increasing separations, as indicated, where reference channel is at  $Z = R = 0$ .

The uncertainties in the cross-correlation estimates are determined by a combination of the statistical error<sup>18</sup> (usually low, <1%) and long range residual common mode correlations. This provides a floor to the measured correlation function and is typically 1%–3%. These residual common mode correlations are calculated with additional channels separated from the main array by 10–15 cm (several times the turbulence correlation length) to monitor for any signal component that is common to the channels over this wider range and, therefore, not attributable to small-scale turbulence.

The uncertainty in the resulting fit function is determined via Monte Carlo error estimation about 1 standard deviation of the fit parameters. The uncertainty in the PSF is determined via a Monte Carlo estimation by varying the local pitch angle and density by 5%–10%, which are the dominant contributions to the uncertainty in the PSF calculation.

This function provides a good fit in one quadrant of the correlation function and can be projected into the other three quadrants based on the fit parameters assuming the turbulence is homogeneous over this range (likely the case in the core, but not necessarily at the edge). This allows for a Fourier transformation without sharp edge artifacts. It should be noted this function is similar to those used on characterizing 2D (poloidal/temporal) edge turbulence data on W-7AS with a tilted structure.<sup>20</sup>

#### IV. RADIAL PROFILE OF TURBULENCE CHARACTERISTICS

Broadband turbulence is observed across the minor radius. The radially and frequency resolved density fluctuation spectrum is shown in Fig. 7(a). The peak of the Doppler-shifted spectrum is noted by squares in the spectrogram in Fig. 7(a). These squares also give the radial location of each measurement. The crosses indicate the centroid frequency of each spectrum, defined as the power weighted average ( $\int f S(f) df / \int S(f) df$ ). Spline interpolation was used to fill in regions of the spectrogram where measurements were not obtained. Low-frequency common-mode signal is present at frequencies below 40 kHz. This is most evident in deep core locations, where the fluctuation levels are small. The fluctuation magnitude is integrated over 40–400 kHz (to avoid common mode signal) and plotted in Fig. 7(b). There is a near monotonic increase in fluctuation magnitude with radius, which is similar to results obtained in L-mode discharges on TFR.<sup>10</sup> Previous measurements in DIII-D L-mode discharges that extend to the plasma edge show the normalized fluctuation amplitude continues to increase upwards of 10%.<sup>8</sup>

Figure 7(c) shows the poloidal wavenumber spectrum normalized to  $\rho_i$ . This spectrum is compensated by deconvolution with the PSF and has been estimated by a 1D fit using simplified version of Eq. (1). The peak wavenumber is observed to remain relatively constant over the entire major radius near  $k_\theta \rho_i = 0.3$ . This is consistent with expectation and simulations of low- $k$  turbulence that predict the ion and electron heat flux to peak near 0.2–0.4  $k_\theta \rho_i$  (thought to be

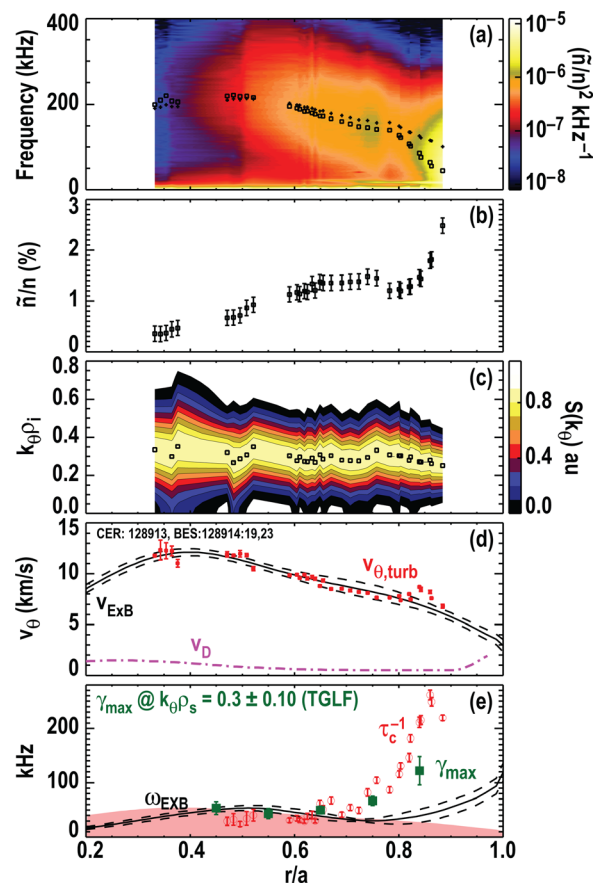


FIG. 7. (Color online) (a) Turbulence profile showing radially and frequency resolved spectrogram, where boxes indicate peak of spectrum and crosses indicate centroid, (b) integrated density fluctuation levels, (c) normalized poloidal wavenumber spectrum, (d)  $E \times B$  velocity calculated via radial force balance (black lines), turbulence group velocity (red points), and diamagnetic velocity (dash-dot-dash), and (e) Hahn-Burrell  $E \times B$  shear rate (black lines) and turbulence decorrelation rate (red points), where the shaded area indicates limited sensitivity.

dominated by ion temperature gradient or trapped electron mode turbulence).<sup>8</sup> The presence of the peak near  $k_\theta \rho_i = 0.3$  is not an artifact of the analysis technique because the BES measurements are sensitive to long-wavelength fluctuations with  $k_\theta \rho_i \leq 1$  and peaks at 0. The width of the spectrum is observed to increase slightly at smaller radii. This reflects a small decrease in the normalized poloidal correlation length,  $L_c / \rho_i$ . The lack of change in the poloidal spatial structure is consistent with previous observations of the poloidal correlation lengths.<sup>21,22</sup> Measurements inside  $r/a < 0.4$  exhibit low fluctuation levels, which inhibits the estimation of the poloidal structure in this region.

Good agreement is found between the  $E \times B$  velocity and the measured turbulence group velocity. This confirms that advection of the broadband turbulence is dominated by the  $E \times B$  flow. Figure 7(d) illustrates the comparison of the BES measured turbulence group velocity in the poloidal direction,  $v_\theta$  (red squares) to the  $E \times B$  velocity (black). The radial electric field is inferred from the impurity (carbon) ion radial force-balance equation using charge exchange recombination (CER) spectroscopy. Here, the dashed black lines indicate the uncertainty in the  $E \times B$  velocity. Turbulence structures are expected to propagate in the plasma frame at a

fraction of the diamagnetic velocity ( $v_D^{e,i} \equiv T_{e,i}/eBL_n$ ), since drift-wave-like instabilities have a central frequency on the order of the diamagnetic frequency.<sup>2</sup> However, it is found that  $v_D^{e,i} < 2$  km/s across the minor radius (purple dashed-dot line), making it a small fraction of the measured turbulence velocity and calculated  $\mathbf{E} \times \mathbf{B}$  velocity. It is difficult to measure a systematic difference in the measured poloidal velocities to determine a turbulence propagation direction in the plasma frame due to the small difference and the experimental uncertainty over most of the profile. 50 ms time windows were analyzed throughout the 400 ms interval window to determine whether time-averaging effects might have hidden this result. This analysis did not indicate a preferred direction over much of the profile. However, in the region outside  $r/a > 0.8$ , there is an observable propagation in the ion-diamagnetic direction outside the experimental uncertainties, seen in Fig. 7(d). This difference is of the same magnitude as the calculated ion diamagnetic drift velocity [purple trace in Fig. 7(d)].

The measured decorrelation rate of the turbulence is compared with the local (Hahm-Burrell)  $\mathbf{E} \times \mathbf{B}$  shearing rate,<sup>23</sup>  $\omega_{\mathbf{E} \times \mathbf{B}}$ . Figure 7(e) shows the radial profile of the measured turbulence decorrelation rate,  $\tau_c^{-1}$  (red points) and,  $\omega_{\mathbf{E} \times \mathbf{B}}$  (black lines). The decorrelation rate is found to be up to 5 times greater than  $\omega_{\mathbf{E} \times \mathbf{B}}$  at  $r/a = 0.9$ , decreases monotonically, and becomes comparable to or less than the  $\omega_{\mathbf{E} \times \mathbf{B}}$  for  $r/a < 0.7$ . The fluctuation levels correlate with  $\tau_c^{-1}$  in that lower turbulence levels are observed when  $\tau_c^{-1}/\omega_{\mathbf{E} \times \mathbf{B}}$  is small. However, the variation in parameters over the minor radius makes it difficult to conclude a meaningful relation to shear suppression theory.

A shaded area below 45 kHz in Fig. 7(e) indicates a region of high uncertainty or a noise floor. Estimations of the decorrelation time in this region require a fit, where  $\tau_c$  is more than four times the maximum measured delay time. This will naturally add large uncertainty in the estimate of  $\tau_c$ . Decorrelation rates measured inside  $r/a \sim 0.6$  are within this high uncertainty region. This indicates the  $\tau_c^{-1}$  is at or below  $\omega_{\mathbf{E} \times \mathbf{B}}$ . Additional poloidally spaced measurements would be needed to measure longer delay times given the high poloidal group velocity [Fig. 7(d)].

The dispersion of the density fluctuations is examined with wavenumber-resolved frequency spectra. This is performed via a 2D transformation of 6 vertical channels to obtain the  $S(k_\theta, f)$  spectrum. This analysis technique is common for measurements with many spatial points, but is coarser given the number BES channels (6) in a vertical array. Given six available channels, there are  $6/2 + 1$  unique  $k_\theta$  spectra. This is shown in Fig. 8 for two cases,  $r/a = 0.6$  and  $r/a = 0.89$ . Each spectrum covers a finite wavenumber range that is centered at the noted  $k_\theta$  and extends roughly  $\pm 0.5 \text{ cm}^{-1}$ . The vertical dotted lines indicate the centroid frequency of each spectrum. The higher wavenumber spectra exhibit a generally Gaussian shape, while the lower wavenumbers have a more complex form. The spectra at  $r/a = 0.89$  show a more positively skewed shape than those at  $r/a = 0.63$ .

There is a 17 kHz peak in Fig. 7(a) at  $r/a > 0.6$ , which corresponds to the density component of the geodesic acoustic mode (GAM).<sup>24</sup> Figure 9 better illustrates this peak

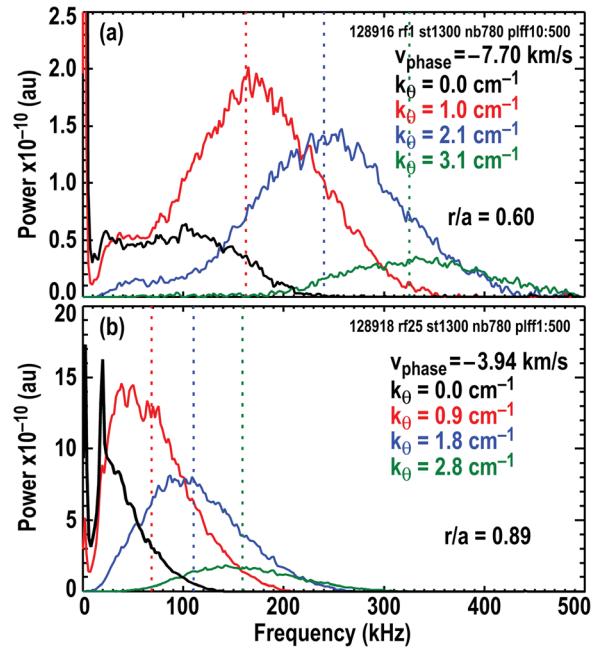


FIG. 8. (Color online) Poloidal wavenumber-resolved power spectra at (a)  $r/a = 0.6$  and (b)  $r/a = 0.9$ .

at higher frequency resolution. The 2D spectrum is shown in Fig. 9(a). The fluctuation levels for the GAM are shown in Fig. 9(b). Individual spectra over seven radii are shown in Fig. 9(c). The dashed line in Fig. 9(a) corresponds to the theoretical GAM frequency defined as  $f_{GAM} \equiv c_s/(2\pi R)$

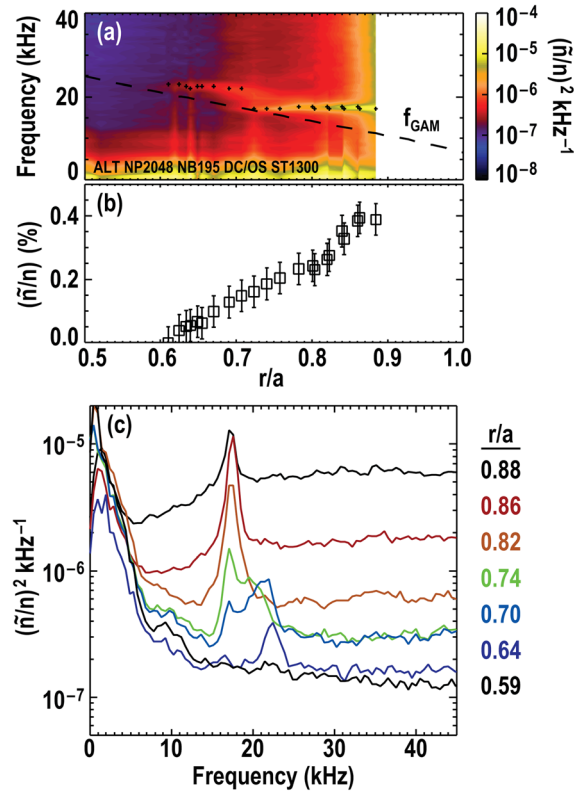


FIG. 9. (Color online) GAM fluctuation spectrum profile (a),  $\bar{n}/n$  levels for GAM component (b), and seven frequency spectra over the radial extent of the GAM (c).

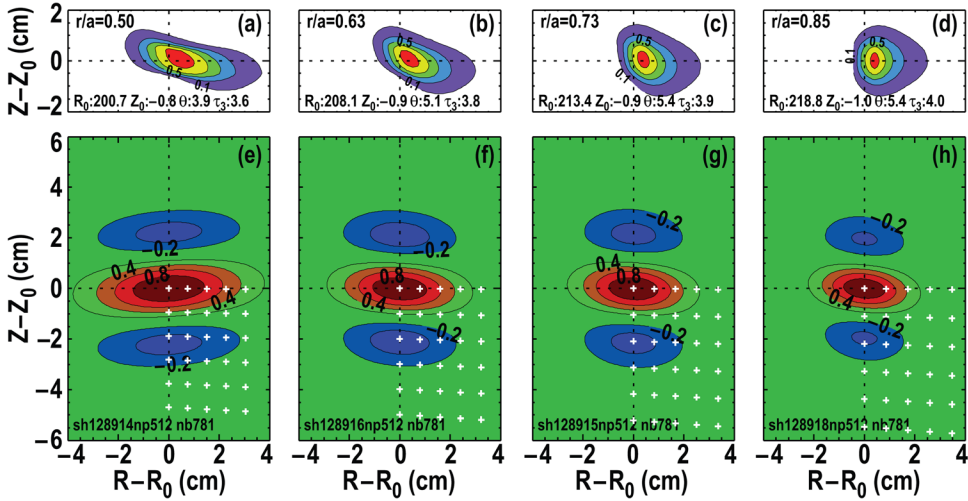


FIG. 10. (Color online) Point spread functions (top row) and raw 2D Correlation function fits (bottom row) at  $r/a = 0.5$  [(a) and (e)],  $r/a = 0.63$  [(b) and (f)],  $r/a = 0.73$  [(c) and (g)], and  $r/a = 0.85$  [(d) and (h)].

$= \sqrt{(T_e + T_i)/m_i}(2\pi R)^{-1}$ .<sup>25</sup> Noncircular shaping will modify this frequency, but that is not taken into account here.

Velocity fluctuation analysis has previously shown the radially sheared GAM zonal flow located outside  $r/a > 0.8$ .<sup>24</sup> The mode is typically found at higher  $q$ , which is why the velocity fluctuations show the edge localization. Here, the GAM has a much deeper radial penetration in the density field.

The GAM is also present in the wavenumber-resolved spectra [Fig. 8(b)] for the spectrum centered at  $k_\theta = 0 \text{ cm}^{-1}$ . The density component of the GAM is expected to have a  $m = 1$  perturbation, where the wavelength is on the order of the plasma height. The plasma elongation,  $\kappa$ , is defined as  $\kappa = b/a$ , where  $a$  is the minor radius and  $b$  is half the height. Thus, the  $m = 1$  perturbation should have a wavenumber on the order:  $k \sim \pi/\kappa a$ . Based on equilibrium reconstructions of this plasma,  $\kappa = 1.6$  and  $a = 64 \text{ cm}$ , which implies the  $m = 1$  perturbation wavenumber is  $k \sim 0.003 \text{ cm}^{-1}$ . The spectrum contains an approximate  $\pm 0.5 \text{ cm}^{-1}$  distribution about  $k_\theta = 0$  which extends beyond the expected wavenumber of the GAM. Therefore, the GAM seen in this low-wavenumber spectrum is consistent with the  $m = 1$  prediction.

The GAM amplitude decays at lower radii and is observed to split at approximately inside  $r/a < 0.75$ . This splitting phenomenon has been seen on TEXTOR (Ref. 26) and is not readily understood. MHD activity is quiet during this analysis period and, thus, is not expected to play a role in this behavior. It is possible that there are two discrete eigenmodes and a different eigenmode may arise deeper in the core where the temperature is higher.

## V. 2D TURBULENCE MEASUREMENTS

Using the techniques described in Sec. II, measurements of the 2D correlation function and wavenumber spectra are obtained over the range of  $0.45 < r/a < 0.9$ . Figure 10 shows the uncompensated/raw correlation functions over this span. The top row [Figs. 10(a)-10(d)] shows the PSF for each channel, and the bottom row [Figs. 10(e)-10(h)] illustrates the respective correlation function at the indicated radii. The white crosses in the lower right quadrant of the

correlation function indicate the locations of measurements used for the correlation function fit [Eq. (1)].

The radial extent of the correlation function is observed to increase toward the core. This effect is a combination of  $\rho_i$  scaling of the radial correlation length<sup>21</sup> and the finite spatial filtering, i.e., the larger the PSF, the larger the apparent correlation function. The poloidal wavenumber shows little change with radius, which is expected from the 1D measurements in Fig. 7(c). A tilt in the correlation function is observed and is found to change with radius, progressing from clockwise to counter-clockwise. This feature is only clearly observed with 2D measurements. It is a relatively minor effect, but is a real effect given the uncertainty of the resulting fit parameters.

These characteristics are likewise found in the transformed  $S(k_r, k_\theta)$  spectra. Figure 11 illustrates the raw and PSF-corrected  $S(k_r, k_\theta)$  spectra for the correlation functions shown in Fig. 10. Here, solid horizontal and vertical lines indicate the maximum in the spectra. The top row [Figs. 11(a)-11(d)] shows the raw spectra, and the bottom row [Figs. 11(e) and 11(f)] shows the corrected spectra. The solid horizontal and vertical lines are duplicated from the raw spectra to show the change with the PSF compensation. The shaded gray regions illustrate the range limits for the PSF compensation, which is defined as the 15% level of the transformed PSF.

The peak in the  $S(k_r, k_\theta)$  spectra is consistently near  $k_\theta = 1.3 \text{ cm}^{-1}$  or  $k_\theta \rho_i = 0.3$  in the  $k_\theta$  direction. The peak in the  $k_r$  direction changes from positive to negative  $k_r$  from the edge to the core, but generally stays near  $k_r = 0$ . This is a direct reflection of the tilted structure observed in the correlation functions; a peak at finite  $k_r$  reflects a tilted/sheared eddy structure. The corrected spectra show a more tilted structure, which indicates that the sample volume effect acts to mask this feature.

The 1D radial and poloidal slices along the horizontal and vertical lines are illustrated in Fig. 12. The limits of the spatial sampling are further illustrated with these slices, where the higher- $k$  regions have significantly higher uncertainty.

Both the radial and poloidal PSF-corrected correlation lengths show an apparent scaling with  $\rho_i$ , which is consistent

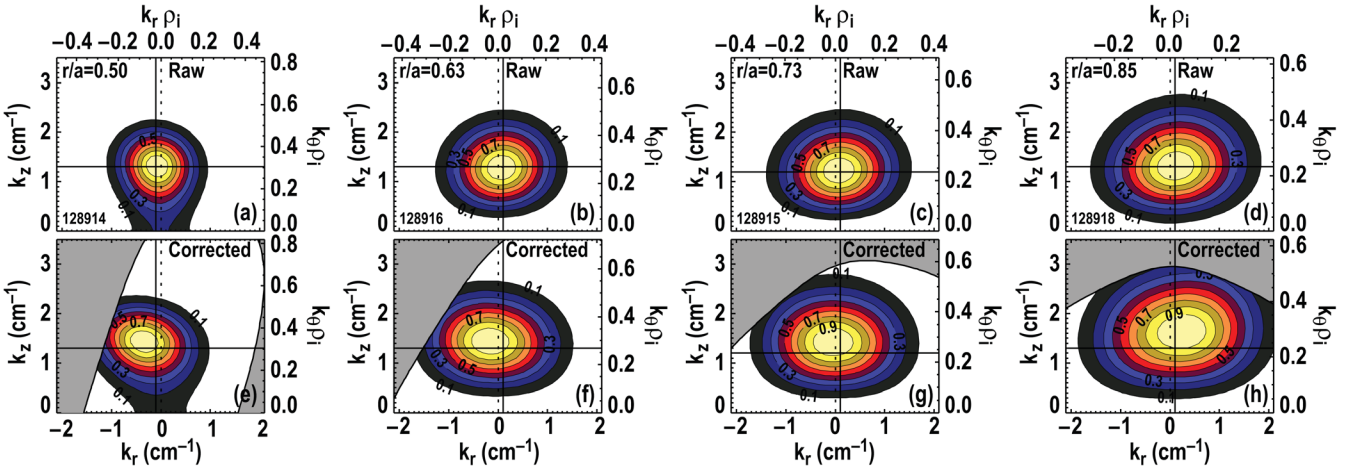


FIG. 11. (Color online) Raw (top row) and compensated (bottom row) 2D wavenumber functions. Gray regions indicate regions outside of measurement sensitivity, estimated as 15% level of STF at  $r/a = 0.5$  [(a) and (e)],  $r/a = 0.63$  [(b) and (f)],  $r/a = 0.73$  [(c) and (g)], and  $r/a = 0.85$  [(d) and (h)].

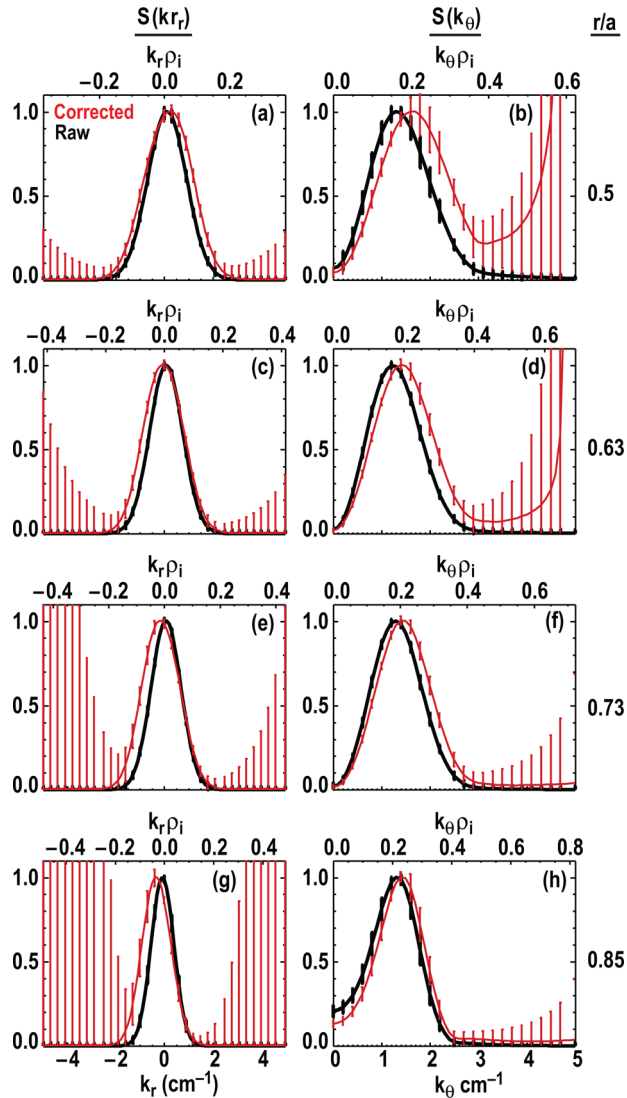


FIG. 12. (Color online) 1D slices of raw (black lines) and compensated (red/gray lines) 2D wavenumber spectra that pass through the maximum of the raw 2D spectrum, which is indicated by the horizontal and vertical lines in Fig. 10.

with previous observations.<sup>21,22,27</sup> Radial and poloidal widths of the corrected spectra are used to estimate correlation lengths ( $L_{c,r}$  and  $L_{c,\theta}$ ). The shifted peak is used to estimate the sheared/tiled structure. Figure 13 illustrates these quantities for the raw (black circles) and corrected (red squares) spectra. This is best illustrated with a dashed line that indicates  $\rho_i$  multiplied by a factor,  $f$ . This multiplication factor has been chosen to minimize the difference between the correlation lengths and  $f\rho_i$ . Here,  $f = 8.9$  for the radial

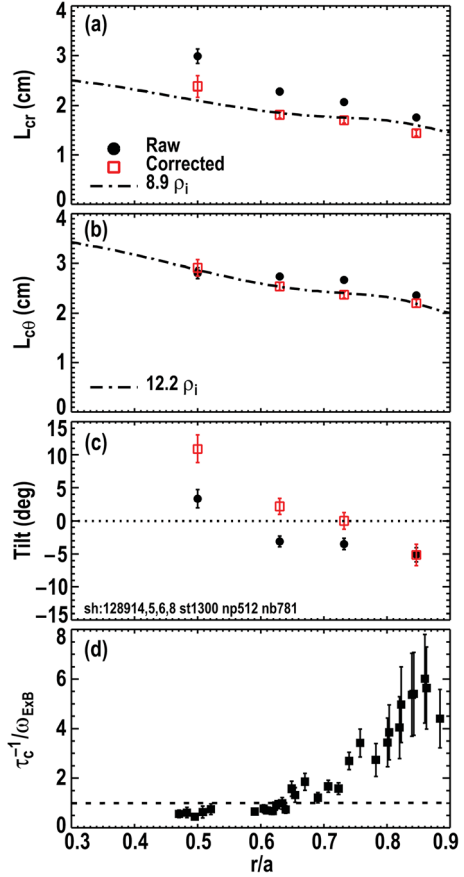


FIG. 13. (Color online) Raw and compensated: radial correlation length (a), poloidal correlation length (b), and tilt angle (c). Dashed lines in (a) and (b) are factors (9.0 and 12.2, respectively) of  $\rho_i$ .

and 12.2 for the poloidal direction. There is good agreement using these multiplication factors indicating a scaling relation. However, this is over a relatively small range of  $\rho_i$ . The difference in  $f$  demonstrates a clear poloidally elongated asymmetry in the time-averaged eddy structure.

A significantly non-zero eddy tilt is observed in the core at  $r/a = 0.5$ , which is consistent with modification resulting from  $\mathbf{E} \times \mathbf{B}$  shear flow. The eddy tilt angle is shown in Fig. 13(c) and is noticeably affected by the PSF correction. It is very plausible that the observed tilt and poloidal elongation result from  $\mathbf{E} \times \mathbf{B}$  shear. Basic considerations in the shear model<sup>28</sup> suggest that the condition  $\omega_{\mathbf{E} \times \mathbf{B}} \geq \tau_c^{-1}$  should approximately hold for  $\mathbf{E} \times \mathbf{B}$  shear to modify the turbulence structure, i.e., if the turbulence decorrelates too quickly for the  $\mathbf{E} \times \mathbf{B}$  shear to tear apart or tilt the eddy, then no shear suppression or tilting would be expected. Therefore, the stronger the relative shear (compared to the decorrelation rate), the greater the ability of the shear to distort and reduce the radial scale. The ratio  $\tau_c^{-1}/\omega_{\mathbf{E} \times \mathbf{B}}$  is shown in Fig. 13(d). The largest tilt angle is observed at the smallest levels of  $\tau_c^{-1}/\omega_{\mathbf{E} \times \mathbf{B}}$ , which is consistent with this simple model. Furthermore, the observed eddy tilt is consistent with the direction of the  $\mathbf{E} \times \mathbf{B}$  flow [Fig. 7(d)].

## VI. COMPARISON TO GYRO SIMULATIONS

Simulations of these L-mode discharges on DIII-D were performed with the GYRO code and compared to measurements of fluctuation levels and 1D spatial characteristics for the discharges presented here at  $r/a = 0.5$  and  $r/a = 0.75$ .<sup>12,13</sup> This analysis applied synthetic diagnostics to the simulation output to allow for direct, quantitative comparison with the experimental BES measurements.<sup>13,29</sup> This synthetic diagnostic accounts for finite spatial resolution of the measurements. For the BES system, the PSF is used as the sample volume in the synthetic diagnostic.

Details of the simulations can be found in Refs. 12 and 13. A brief summary of these results is presented here. At  $r/a = 0.5$ , frequency spectra, fluctuation levels, and 1D correlation functions show generally good agreement between measurement and synthetic diagnostic analysis. The GYRO predicted ion and electron heat fluxes also agree well with the calculated fluxes via power balance. However, at  $r/a = 0.75$ , the simulation under predicts the heat flux by a factor of 7 and fluctuation amplitude levels by a factor of 3 (fluctuation power by a factor of 9). The frequency resolved spectra for measurement and simulation show the fluctuation level discrepancy at  $r/a = 0.75$  in Fig. 14. The 1D correlation functions show reasonable agreement between measurement and synthetic diagnostic analysis of the turbulence spatial structure.

Comparisons of the 2D fluctuation structure can provide additional crucial details that could be overlooked with the 1D measurements. Here, the GYRO density fluctuation results are converted to lab-frame coordinates in a set of grid points that match the BES array dimensions.<sup>13</sup> The array of points is used to compute 2D correlation functions. The model function from Eq. (1) is not used with the GYRO results.

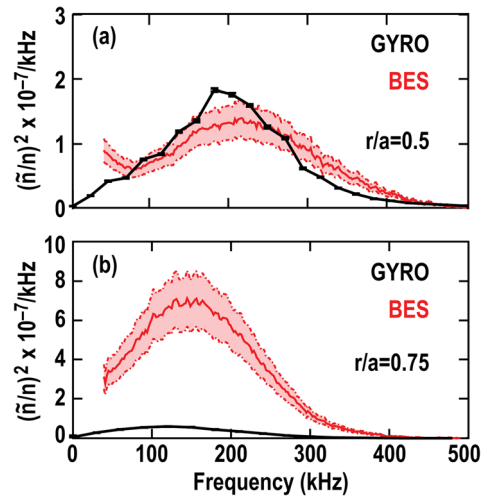


FIG. 14. (Color online) Frequency resolved spectra from BES (red/gray) and GYRO with synthetic BES diagnostic applied (black lines) at (a)  $r/a = 0.5$  and (b)  $r/a = 0.75$ . [Reprinted with permission from C. Holland *et al.*, Phys. Plasmas 16, 052301 (2009). Copyright © 2010, American Institute of Physics.]

Figure 15 illustrates the density fluctuation correlation functions calculated from GYRO simulations with the raw output [(a) and (b)] and with the synthetic diagnostic [(c) and (d)] for both radial locations. The finite spatial sampling effect from the PSF is readily seen from these results, where the synthetic correlation function is larger than that of the raw GYRO simulations [comparing Figs. 15(a) to 15(b) and 15(c) to 15(d)].

The overall structure is similar to that in Fig. 10 for the BES data. There are, however, some systematic differences in the details. At  $r/a = 0.5$ , the poloidal structure for the synthetic GYRO result has a larger overall envelope and has

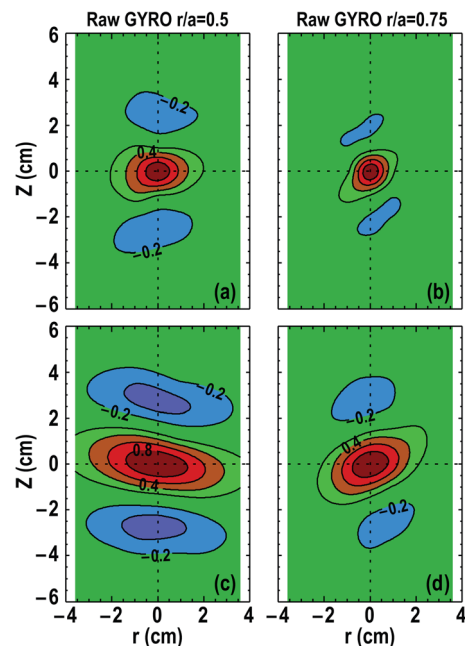


FIG. 15. (Color online) Density fluctuation correlation functions via GYRO simulations at  $r/a = 0.5$  [(a) and (c)] and  $r/a = 0.75$  [(b) and (d)] for the raw output [(a) and (b)] and with the synthetic BES diagnostic applied [(c) and (d)].

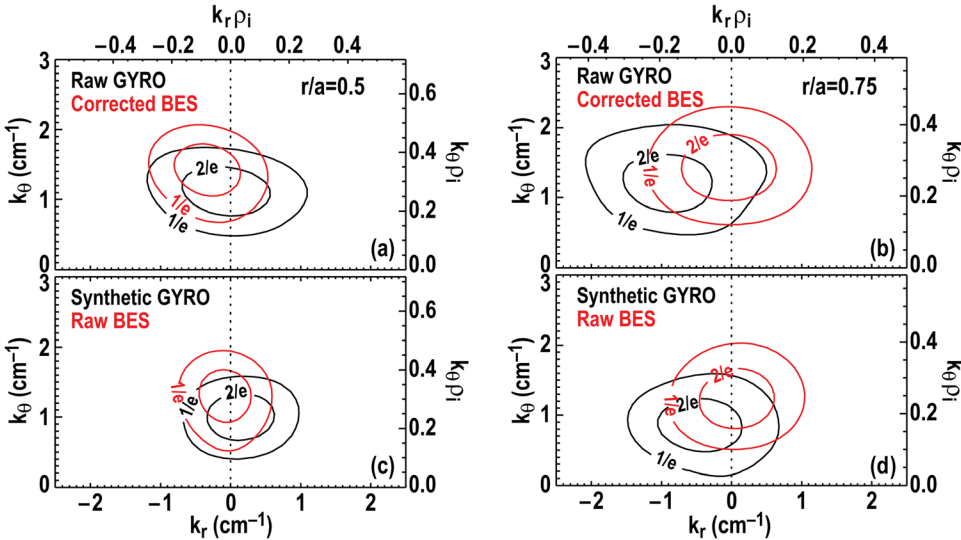


FIG. 16. (Color online) Comparison of 2D wavenumber structure via GYRO simulations (black lines) and BES measurements (red/gray lines) at  $r/a = 0.5$  [(a) and (c)] and  $r/a = 0.75$  [(b) and (d)].

a smaller  $k_\theta$  compared to the raw correlation function in Fig. 10. The differences are small. Disagreement is more apparent at  $r/a = 0.75$ . Here, the shear angle from the GYRO data is observed to be  $30^\circ$ – $35^\circ$ , which is much larger than the uncompensated measured angle which is near  $0^\circ$ .

The transformed  $S(k_r, k_\theta)$  spectra for both radial positions are shown in Fig. 16. The relevant quantities to compare are the synthetic GYRO spectra with the raw BES and, conversely, the corrected BES with the raw GYRO spectra. For simplicity, only two contour levels for each spectrum are shown. Ideally, the corrected BES functions should be compared to the raw GYRO output. This should allow the clearest picture of the turbulence. However, the corrected BES spectra are limited at higher wavenumbers due to a sensitivity limit. Thus, the synthetic GYRO and raw BES are also shown for completeness.

Looking first at the  $r/a = 0.5$  case in Fig. 16, both the raw and compensated BES measured spectra indicate a larger absolute peak  $k_r$  than the GYRO simulations. This indicates a sheared eddy structure from the BES measurements that is not seen in the simulations (which include the full  $\mathbf{E} \times \mathbf{B}$  velocity and shear values). However, comparing the raw BES measurements to the synthetic GYRO simulations, the peak  $k_r$  are both near  $0\text{ cm}^{-1}$ . As noted above, the PSF pushes  $k_r$  to 0. The raw GYRO radial width is 30% larger than the compensated BES, indicating a smaller radial correlation. The disagreement is closer to 20% for the raw BES and synthetic GYRO. In the poloidal direction, the widths are more in agreement for both cases. However, there

is a noticeable 30% larger peak  $k_\theta$  in the measurement compared to the simulation, consistent with previous 1D studies.<sup>13</sup> The structure shows good agreement, despite these small differences.

The  $r/a = 0.75$  case shows similar or better agreement in the radial and poloidal widths and the peak  $k_\theta$ . The peak  $k_r$ , however, is significantly different. The large absolute peak  $k_r$  in the simulation results in a significant oscillation in the radial direction that gives the apparent sheared eddy structure in the correlation function. The fact that the predicted turbulence structure extends to higher wavenumber than that of the measured BES spectra may help explain why the GYRO simulations under-predict the transport at this radial location. An exaggerated  $\mathbf{E} \times \mathbf{B}$  shear would be expected to suppress low wavenumber structures and distort the turbulent eddies. This, in turn, would be expected to lower the transport, which is seen. If the shear was exaggerated, these effects seen would be expected. This interpretation is speculative, but consistent with the data.

Overall, main features of the 2D spectra compare well at both locations, but differences are observed, with the larger difference at  $r/a = 0.75$ . This is not unexpected considering the small tilted structure observed at  $r/a = 0.75$  (Fig. 15).

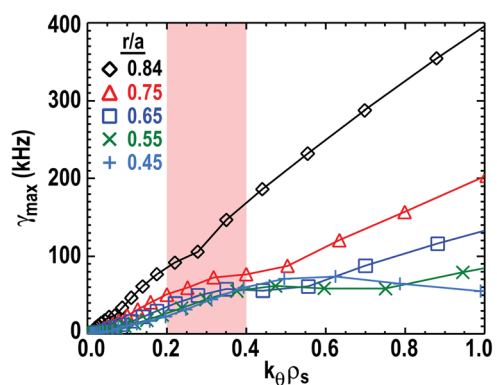


FIG. 17. (Color online) Maximum linear growth rates calculated from TGLF, and region of peak wavenumber spectra as measured with BES (shaded area).

TABLE I.  $r/a = 0.5$  case.

	$k_r$ width (cm <sup>-1</sup> )	$k_\theta$ width (cm <sup>-1</sup> )	$k_r$ peak (cm <sup>-1</sup> )	$k_\theta$ peak (cm <sup>-1</sup> )
Compensated BES	1.7	1.4	-0.4	1.4
Raw GYRO	2.2	1.3	-0.1	1.1
Raw BES	1.3	1.4	-0.1	1.3
Synthetic GYRO	1.6	1.2	0.2	1.0

TABLE II.  $r/a = 0.75$  case.

	$k_r$ width (cm $^{-1}$ )	$k_\theta$ width (cm $^{-1}$ )	$k_r$ peak (cm $^{-1}$ )	$k_\theta$ peak (cm $^{-1}$ )
Compensated BES	2.4	1.7	-0.1	1.4
Raw GYRO	2.5	1.5	-1.0	1.2
Raw BES	2.0	1.5	-0.5	1.3
Synthetic GYRO	2.2	1.5	0.1	0.9

Tables I and II summarize the widths and peaks for the 2D spectra shown in Fig. 16.

## VII. COMPARISON OF GROWTH RATES TO DECORRELATION RATE

The trapped gyro-Landau-fluid code (TGLF)<sup>30</sup> is used to calculate the maximum linear growth rates of the most unstable turbulence modes for these plasmas.<sup>12</sup> Figure 17 illustrates the growth rate spectrum at 5 radii. This covers ITG and TEM scales, where the higher wavenumbers correspond to TEM modes.

The BES-measured  $S(k_\theta)$  spectra shown in Figs. 11(c) indicate a peak that is constant near  $k_\theta \rho_i = 0.3$ . There is some distribution over neighboring wavenumbers, but the bulk of the power is approximately  $k_\theta \rho_i = 0.3 \pm 0.1$ . This range is shaded on Fig. 17. Here, the wavenumbers are normalized to  $\rho_s = \sqrt{m_i T_e} / eB \approx \rho_i$ , given  $T_i \approx T_e$  over the measurement range [shown in Fig. 2(a)].

The maximum linear growth rates,  $\gamma_{\max}$ , are averaged over this wavenumber range and plotted in Fig. 7(e) as green squares. The error bar represents the standard deviation in wavenumbers over the range averaged. This shows that there is good agreement between the measured nonlinear decorrelation rate,  $\tau_c^{-1}$ , and  $\gamma_{\max}$ , where both quantities rise toward the edge. The maximum linear growth rate is often compared to the  $\mathbf{E} \times \mathbf{B}$  shear rate in order to determine when a turbulence suppression mechanism is active, as it is typically easier to calculate  $\gamma_{\max}$  than to measure  $\tau_c^{-1}$ . This provides a valuable check on this theory and approach to analyzing shear suppression.

## VIII. CONCLUSIONS

A quantitative description of the 1D and 2D localized characteristics of turbulence in L-mode discharges on DIII-D has been presented. Long-wavelength broadband turbulence is observed throughout the core of these L-mode plasmas. Fluctuation levels increase from less than 0.3% at  $r/a = 0.35$  to greater than 2.5% at  $r/a = 0.9$ . The measured decorrelation rate is found to be less than 45 kHz inside  $r/a \sim 0.6$  where it is comparable to or less than the  $\mathbf{E} \times \mathbf{B}$  shear rate. Outside  $r/a \sim 0.8$  (in regions of higher fluctuation levels), the decorrelation rate is found to exceed the  $\mathbf{E} \times \mathbf{B}$  shear rate by up to a factor of five. The poloidal group velocity is found to agree well with  $\mathbf{E} \times \mathbf{B}$  the velocity. This confirms that the  $\mathbf{E} \times \mathbf{B}$  velocity dominates the poloidal advection of the turbulence.

The ensemble-averaged 2D turbulence structure in real and wavenumber space was shown for  $0.45 < r/a < 0.9$ .

The PSF-corrected eddy structure size is found to scale with the ion gyroradius over a small range in  $\rho_i$  and exhibits an elongated poloidal asymmetry. A sheared eddy structure is observed and is found to vary with radius. The most tilted structure is observed in the region with lowest fluctuation levels and decorrelation rates. Both the elongated and tilted structures are consistent with expectations and concepts from the model for  $\mathbf{E} \times \mathbf{B}$  shear suppression.

The 2D structure has further been compared to nonlinear simulations with the GYRO code at two radii, 0.5 and 0.75. Overall, the simulations have shown good general agreement with the measured structures.<sup>13</sup> There are, however, pertinent differences in the details. The most significant difference is the predicted sheared structure and peak  $k_r$  that is not observed in the measurements at  $r/a = 0.75$ . This implies a larger than observed impact from shear implemented in the simulations, which may be responsible for the underpredicted fluctuation levels and transport fluxes. It is not unexpected that simulations in this region are more difficult as the more complex turbulent edge mixes with the core. Simulating the outer regions is a greater challenge for turbulence simulations due to geometrical effects and more sharply varying spatial gradients. This is of great interest for coupling the core and the edge. The maximum linear growth rates are found to closely agree with the measured decorrelation rates, which provide a good check for using  $\gamma_{\max}$  with shear suppression theory.

## ACKNOWLEDGMENTS

The authors thank K. Burrell, R. Waltz, and J. Candy for useful discussions, and the DIII-D program for its support of this collaborative research program. This work supported in part by the U.S. Department of Energy under DE-FG02-08ER54999, DE-FG02-89ER53296, DE-FG02-07ER54917, DE-AC05-06OR23100, and DE-FC02-04ER54698.

- <sup>1</sup>G. R. Tynan, A. Fujisawa, and G. R. McKee, *Plasma Phys. Controlled Fusion* **51**, 113001 (2009).
- <sup>2</sup>W. Horton, *Rev. Mod. Phys.* **71**, 735 (1999).
- <sup>3</sup>A. J. Wootton, B. A. Carreras, H. Matsumoto, K. McGuire, W. A. Peebles, Ch. P. Ritz, P. W. Terry, and S. J. Zweben, *Phys. Fluids B* **2**, 2879 (1990).
- <sup>4</sup>S. J. Zweben, D. P. Stotler, J. L. Terry, B. LaBombard, M. Greenwald, M. Muterspaugh, C. S. Pitcher, K. Hallatschek, R. J. Maqueda, B. Rogers, J. L. Lowrance, V. J. Mastrocola, and G. F. Renda, *Phys. Plasmas* **9**, 1981 (2002).
- <sup>5</sup>S. J. Zweben and R. W. Gould, *Nucl. Fusion* **25**, 171 (1985).
- <sup>6</sup>A. Fasoli, B. Labit, M. McGrath, S. H. Muller, G. Plyushchev, M. Podesta, and F. M. Poli, *Phys. Plasmas* **13**, 055902 (2006).
- <sup>7</sup>P. Manz, M. Ramisch, U. Stroth, V. Naulin, and B. D. Scott, *Plasma Phys. Controlled Fusion* **50**, 035008 (2008).
- <sup>8</sup>G. R. McKee, R. J. Fonck, D. K. Gupta, D. J. Schlossberg, M. W. Shafer, R. L. Boivin, and W. M. Solomon, *J. Plasma Fusion Res.* **2**, S1025 (2007).
- <sup>9</sup>R. J. Fonck, N. Bretz, G. Cosby, R. Durst, E. Mazzucato, R. Nazikian, S. Paul, S. Scott, W. Tang, and M. Zamstorff, *Plasma Phys. Controlled Fusion* **34**, 1993 (1992).
- <sup>10</sup>R. J. Fonck, G. Cosby, R. D. Durst, S. F. Paul, N. Bretz, S. Scott, E. Synakowski, and G. Taylor, *Phys. Rev. Lett.* **70**, 3736 (1993).
- <sup>11</sup>J. Candy and R. E. Waltz, *J. Comput. Phys.* **186**, 545 (2003).
- <sup>12</sup>A. E. White, L. Schmitz, G. R. McKee, C. Holland, W. A. Peebles, T. A. Carter, M. W. Shafer, M. E. Austin, K. H. Burrell, J. Candy, J. C. DeBoo, E. J. Doyle, M. A. Makowski, R. Prater, T. L. Rhodes, G. M. Staebler, G. R. Tynan, R. E. Waltz, and G. Wang, *Phys. Plasmas* **15**, 056116 (2008).
- <sup>13</sup>C. Holland, A. E. White, G. R. McKee, M. W. Shafer, J. Candy, R. E. Waltz, L. Schmitz, and G. R. Tynan, *Phys. Plasmas* **16**, 052301 (2009).

- <sup>14</sup>R. J. Fonck, P. A. Duperrex, and S. F. Paul, *Rev. Sci. Instrum.* **61**, 3487 (1990).
- <sup>15</sup>M. W. Shafer, R. J. Fonck, G. R. McKee, and D. J. Schlossberg, *Rev. Sci. Instrum.* **77**, 10F110 (2007).
- <sup>16</sup>I. H. Hutchinson, *Plasma Phys. Controlled Fusion* **44**, 71 (2002).
- <sup>17</sup>R. D. Durst, R. J. Fonck, G. Cosby, H. Evensen, and S. F. Paul, *Rev. Sci. Instrum.* **63**, 4907 (1992).
- <sup>18</sup>J. S. Bendat and A. G. Piersol, *Random Data* (Wiley, New York, 2000).
- <sup>19</sup>C. B. Markwardt, "Non-Linear Least Squares Fitting in IDL with MPFIT," in *Proc. Astronomical Data Analysis Software and Systems XVIII, Quebec, Canada, ASP Conference Series*, Vol. 411, edited by D. Bohlender, P. Dowler, and D. Durand (Astronomical Society of the Pacific, San Francisco, CA, 2008), pp. 251–254.
- <sup>20</sup>J. Bleuel, M. Endler, H. Niedermeyer, M. Schubert, H. Thomsen, and W7-AS Team, *New J. Phys.* **4**, 38 (2002).
- <sup>21</sup>G. R. McKee, C. C. Petty, R. E. Waltz, C. Fenzi, R. J. Fonck, J. E. Kinsey, T. C. Luce, K. H. Burrell, D. R. Baker, E. J. Doyle, X. Garbet, R. A. Moyer, C. L. Rettig, T. L. Rhodes, D. W. Ross, G. M. Staebler, R. Sydora, and M. R. Wade, *Nucl. Fusion* **41**, 1235 (2001).
- <sup>22</sup>M. Ramisch, N. Mahdizadeh, U. Stroth, F. Greiner, C. Lechte, and K. Rahbarnia, *Phys. Plasmas* **12**, 032504 (2005).
- <sup>23</sup>K. H. Burrell, *Phys. Plasmas* **4**, 1499 (1997).
- <sup>24</sup>G. R. McKee, R. J. Fonck, M. Jakubowski, K. H. Burrell, K. Hallatschek, R. A. Moyer, D. L. Rudakov, W. Nevins, G. D. Porter, P. Schoch, and X. Xu, *Phys. Plasmas* **10**, 1712 (2003).
- <sup>25</sup>N. Winsor, J. L. Johnson, and J. M. Dawson, *Phys. Fluids* **11**, 2448 (1968).
- <sup>26</sup>A. Kramer-Flecken, S. Soldatov, D. Reiser, M. Kantor, and H. R. Koslowski, *Plasma Phys. Controlled Fusion* **51**, 015001 (2009).
- <sup>27</sup>T. L. Rhodes, J.-N. Leboeuf, R. D. Sydora, R. J. Groebner, E. J. Doyle, G. R. McKee, W. A. Peebles, C. L. Rettig, L. Zeng, and G. Wang, *Phys. Plasmas* **9**, 2141 (2002).
- <sup>28</sup>P. W. Terry, *Rev. Mod. Phys.* **72**, 109 (2000).
- <sup>29</sup>R. V. Bravenc and W. M. Nevins, *Rev. Sci. Instrum.* **77**, 015101 (2006).
- <sup>30</sup>G. M. Staebler, J. E. Kinsey, and R. E. Waltz, *Phys. Plasmas* **14**, 055909 (2007).